STATISTICS, OPTIMIZATION AND INFORMATION COMPUTING
Stat., Optim. Inf. Comput., Vol. **x**, Month 202x, pp 0–21.
Published online in International Academic Press (www.IAPress.org)

Influence of Urban Obstacles on Reactive NO_2–O_3 Transport in a Tropical Street Canyon Using the k-ω SST Model

Rachmanu Eko Handriyono [1,3], Basuki Widodo [2], Abdu Fadli Assomadi [1], Arie Dipareza Syafei [1], Joni Hermana [1,*]

[1] *Department of Environmental Engineering, Institut Teknologi Sepuluh Nopember, Surabaya, Indonesia*
[2] *Department of Mathematics, Institut Teknologi Sepuluh Nopember, Surabaya, Indonesia*
[3] *Department of Environmental Engineering, Institut Teknologi Adhi Tama Surabaya, Indonesia*

Abstract Urban street canyons in tropical regions tend to experience pollutant accumulation due to complex urban geometries and atmospheric chemical transformation processes. This study investigates the influence of urban obstacles, including buildings and simplified roadside obstacles, on the reactive transport of NO_2–O_3 within a tropical street canyon using Computational Fluid Dynamics (CFD). The CFD framework is based on the Reynolds-Averaged Navier–Stokes (RANS) equations with the k-ω Shear Stress Transport (SST) turbulence model. The case study was conducted along Dr. Ir. H. Soekarno Street, East Surabaya, Indonesia, incorporating NO_2 photolysis and subsequent gas-phase reactions leading to the formation of O_3 and NO, thereby representing a non-conservative pollutant system. Simulation results indicate that the presence of obstacles alters the airflow structure within the street canyon, characterized by the development of high-pressure zones on the windward side of buildings and weakened airflow in the mid-canyon region. The concentration fields further show that the simplified obstacle configuration influences local ventilation and the spatial distribution of reactive pollutants NO_2 and O_3. It should be noted that the roadside obstacle elements were represented as simplified solid barriers, and thus the model does not explicitly resolve porous vegetation effects such as canopy drag, turbulence generation, or pollutant deposition. The integration of non-conservative atmospheric chemistry within the CFD model provides insight into NO_2–O_3 interaction dynamics under the obstacle configuration. Overall, the model achieved numerical convergence and remained stable throughout the simulation, demonstrating its capability to represent the effects of simplified urban obstacle on pollutant transport under the examined conditions.

Keywords Reactive Pollutant Transport, simplified roadside obstacles, Street Canyon, Urban Obstacles

DOI: 10.19139/soic-2310-5070-3270

1. Introduction

Air quality in tropical urban areas is influenced by anthropogenic activities, meteorological conditions, and complex urban geometries [1, 2, 3]. Its adverse effects may develop over time and are often difficult to assess comprehensively [4]. In street canyon environments, interactions among opposing building facades, roadside green spaces, and local wind patterns often result in restricted air circulation, thereby increasing the potential accumulation of reactive pollutants near the road surface [5, 6, 7, 8]. This condition is further complicated by atmospheric chemical transformations, particularly involving nitrogen oxides (NO_x) and ozone (O_3), which are strongly influenced by solar radiation intensity and turbulence dynamics [9, 10]. As one of the major transportation corridors in Surabaya, Dr. Ir. H. Soekarno Street provides a representative case for investigating the interaction between street-canyon geometry and reactive pollutant transport.

*Correspondence to: Joni Hermana (Email: hermana@its.ac.id). Department of Environmental Engineering, Institut Teknologi Sepuluh Nopember, Surabaya, East Java, Indonesia (60111).

ISSN 2310-5070 (online) ISSN 2311-004X (print)

Nitrogen dioxide (NO_2) is one of the primary pollutants emitted from motor vehicles and is highly reactive once released into the atmosphere. NO_2 can undergo photolysis to form nitrogen monoxide (NO) and atomic oxygen, which subsequently contribute to tropospheric ozone formation through a series of gas-phase reactions [10, 11]. In tropical regions such as Surabaya, high solar irradiance and distinct meteorological characteristics play a critical role in accelerating NO_2 photochemical reactions [12]. The presence of urban obstacles such as buildings and vegetation also influences airflow patterns and ventilation within street canyons [13, 14, 15]. Buildings act as physical barriers that can generate stagnation zones, pressure gradients, and recirculation patterns [16, 17], while vegetation may either enhance or reduce local turbulence and affect the deposition and dispersion of reactive pollutants [18, 19]. Although various air quality models such as AERMOD, CALPUFF, and WRF-Chem have been widely used to predict urban pollution, these models generally focus on physical transport and do not explicitly integrate obstacle effects or non-conservative chemical reactions at the street scale [20, 21].

Computational Fluid Dynamics (CFD) is well suited for this purpose because it can resolve airflow and pollutant dispersion at high spatial resolution in complex urban geometries [22, 23, 24, 25]. When implemented within a Reynolds-Averaged Navier–Stokes (RANS) framework, CFD provides a practical balance between computational cost and predictive capability for urban environmental applications [26]. Among available turbulence closures, the k–ω Shear Stress Transport (SST) model is widely used for urban-flow simulation because it performs well in regions with strong shear, wall effects, and flow separation [27, 28].

Although numerous studies have examined pollutant dispersion in street canyons, most previous works have primarily focused on either physical transport processes or simplified reactive mechanisms, with relatively few studies simultaneously considering obstacle-induced flow modification and reactive NO_2–O_3 chemistry in tropical urban environments. Existing studies are particularly limited in integrating these aspects under meteorological conditions typical of Indonesia, especially in Surabaya. In this study, the roadside green-strip elements observed in the real street canyon are represented in the CFD model as simplified solid obstacle regions, providing a controlled framework to isolate the primary influence of obstacle presence on the coupled flow–chemistry system without explicitly resolving porous vegetation dynamics. This study addresses that gap by integrating non-conservative photochemical reactions with obstacle-induced airflow modifications in CFD simulations under typical meteorological conditions in Surabaya. Therefore, this study aims to analyze the influence of urban obstacles on airflow patterns and the distribution of reactive NO_2–O_3 pollutants in a tropical street canyon using the k–ω SST turbulence model. The main contribution of this study is the coupling of a CFD-based RANS framework with a simplified reactive chemistry scheme to examine how obstacle-modified airflow affects NO_2–O_3 dynamics under tropical conditions, with relevance to urban air quality assessment in tropical cities.

2. Methods

2.1. Study Area and Domain Configuration

The study was conducted using a representative tropical street canyon located along Dr. Ir. H. Soekarno Street in East Surabaya, Indonesia (7°18′49.07″S, 112°46′50.56″E). This study used average meteorological data from January to March 2024, corresponding to the rainy season. The meteorological data used in this study were obtained from the BMKG Juanda station, the nearest meteorological station to the study area. Ambient air quality data were obtained from the SUF 6 air quality monitoring station located in Wonorejo, Surabaya. These data provided essential input for the simulation, including parameters such as wind speed, temperature, and solar radiation, which are critical for accurate CFD modeling of the street canyon environment. The area is characterized by high traffic density and the presence of buildings and roadside vegetation (represented as simplified obstacles in the CFD model) that form a semi-enclosed urban canyon. Fig. 1 illustrates the location of the simulation domain.

The canyon consists of two parallel road segments bounded by two rows of buildings and flanked by roadside vegetation. Each building block measures 185 m in length, 30 m in width, and 15 m in height. Three vegetated strips are positioned between and beside the road segments, with widths of 5 m, 8 m, and 5 m, respectively. In the present CFD model, these vegetated strips are represented as simplified solid obstacle regions to isolate the primary aerodynamic effect of obstacle presence, rather than explicitly resolving porous vegetation behavior. The

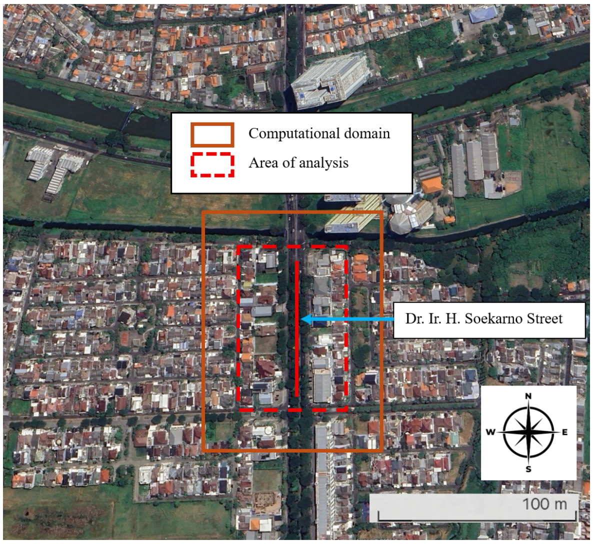

Figure 1. Location of the study area

computational domain extends 245 m in the streamwise direction, 124 m laterally, and 60 m vertically to minimize blockage effects and ensure a realistic representation of the approaching airflow (Fig. 2 and 3). This domain size satisfies common best-practice recommendations for CFD simulations of urban street canyons.

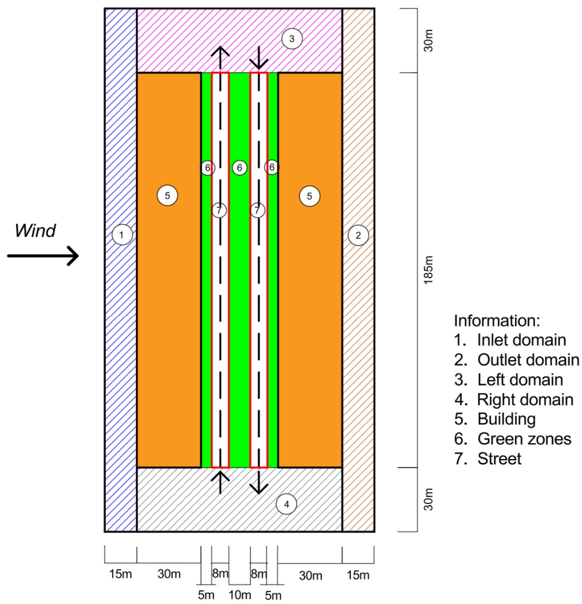

Figure 2. Street canyon geometry at the study location, top view

2.2. *Governing equations and turbulence modeling*

In this study, Computational Fluid Dynamics (CFD) was used to simulate the behavior of atmospheric airflow within an urban street canyon. The simulations were performed using ANSYS Fluent 2024 R2, licensed through

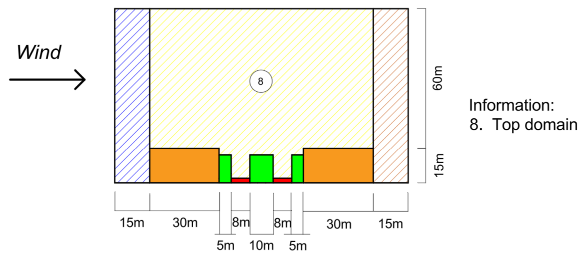

Figure 3. Street canyon geometry at the study location, side view

Institut Teknologi Sepuluh Nopember (ITS), Surabaya. Airflow transports mass, momentum, and energy, and its motion is governed by the fundamental conservation laws of mass, momentum, and energy. The conservation of mass ensures that no artificial mass is created or lost within the computational domain. When air flows between two opposing buildings forming a street canyon, no new air spontaneously appears or disappears; therefore, mass continuity must be satisfied. Similarly, the airflow within the canyon is subjected to external forcing from the incoming wind, resistive forces from building surfaces, and viscous shear between fluid layers. These interactions require the conservation of momentum to determine the resulting velocity and pressure fields.

Furthermore, because this study examines reactive transport involving non-conservative gas species, the conservation of energy is also relevant. Energy affects temperature, density, viscosity, and chemical reaction rates, particularly the photochemical transformation of NO_2. The governing conservation equations for mass, momentum, and energy are expressed as follows [29, 30].

Mass conservation:

$$\frac{\partial \rho}{\partial t} + \nabla \cdot (\rho u_i) = 0 \tag{1}$$

Momentum conservation:

$$\frac{\partial}{\partial t}(\rho u_i) + \nabla \cdot (\rho u_i u_j) = -\nabla P + \nabla \cdot \tau + \rho g \tag{2}$$

Energy conservation:

$$\frac{\partial (\rho h)}{\partial t} + \nabla \cdot (\rho u_j h) = \nabla \cdot (k_{t,\text{eff}} \nabla T) + S_h \tag{3}$$

Where:

$$h = C_p T \tag{4}$$

$$k_{t,\text{eff}} = k_t + \frac{\mu_t C_p}{Pr} \tag{5}$$

$$S_h = \alpha_{\text{abs}} \cdot I \tag{6}$$

The variables in Eqs. (1)–(6) are defined as follows: ρ is the air density (kg/m^3); u_i ($i = x, y, z$) denotes the velocity components (m/s); P is the static pressure (Pa); τ is the viscous stress tensor (N/m^2); g is the gravitational acceleration (m/s^2); h is the specific enthalpy (J/kg); C_p is the specific heat at constant pressure (J/kg·K); T is the temperature (K); $k_{t,\text{eff}}$ is the effective thermal conductivity (W/m·K); μ_t is the turbulent viscosity (kg/m·s); Pr is the Prandtl number; S_h is the volumetric heat source term representing solar radiative heating (W/m^3); α_{abs} is the effective volumetric absorption coefficient (m^{-1}), representing the fraction of incident solar energy absorbed per unit depth of the air column or road surface; and I is the incident solar radiation intensity at the surface (W/m^2), obtained from field measurements at the BMKG Juanda station during the study period.

The volumetric heat source term S_h in Eq. (6) represents the conversion of absorbed solar radiation into thermal energy within the computational domain. This formulation follows the approach commonly adopted in urban CFD energy models, in which the incident solar flux I is scaled by an effective absorption coefficient α_{abs} to yield a volumetric source term consistent with the energy conservation equation [28]. In the present study, α_{abs} was set to $1/L_z$, where L_z denotes the vertical extent of the domain (60 m), assuming a uniform distribution of solar heating across the full domain height. This is equivalent to treating the absorbed solar energy as uniformly distributed over the vertical column of the computational domain, providing a simplified but physically consistent representation of the solar heating effect on the canyon air temperature. It is acknowledged that this assumption does not resolve the vertical profile of radiative absorption or the effect of building shadowing, and therefore represents a limitation of the present thermal formulation.

Turbulent flows contain kinetic energy associated with small-scale velocity fluctuations, which evolve through production and dissipation mechanisms. To represent these effects, the turbulent kinetic energy equation accounts for the generation of turbulence by mean shear, while the specific dissipation rate equation describes the viscous dissipation of turbulent energy into heat. This study employs the k–ω Shear Stress Transport (SST) turbulence model, which is specifically designed for flows characterized by steep velocity gradients, flow separation, and strong shear, all of which commonly arise in urban street canyons. The SST model combines the advantages of the k–ω model near wall surfaces, where accurate near-wall resolution can be achieved without wall functions, with the stability of the k–ε model in free-stream regions through a blending function [27]. The governing transport equations of the SST model are given below.

Turbulent kinetic energy equation (k)

$$\frac{\partial(\rho k)}{\partial t} + \frac{\partial(\rho u_j k)}{\partial x_j} = P_k - \rho\beta^* k\omega + \frac{\partial}{\partial x_j}\left[(\mu + \sigma_k \mu_t)\frac{\partial k}{\partial x_j}\right] \tag{7}$$

Specific dissipation rate equation (ω)

$$\frac{\partial(\rho \omega)}{\partial t} + \frac{\partial(\rho u_j \omega)}{\partial x_j} = \alpha\frac{\omega}{k}P_k - \beta\rho\omega^2 + \frac{\partial}{\partial x_j}\left[(\mu + \sigma_\omega \mu_t)\frac{\partial \omega}{\partial x_j}\right] + 2(1-F_1)\rho\sigma_{\omega 2}\frac{1}{\omega}\frac{\partial k}{\partial x_j}\frac{\partial \omega}{\partial x_j} \tag{8}$$

Where:

$$P_k = 2\mu_t S_{ij} S_{ij} \tag{9}$$

$$\mu_t = \rho a_1 \frac{k}{\max(a_1\omega,\, SF_2)} \tag{10}$$

$$S = \sqrt{2S_{ij}S_{ij}} \tag{11}$$

The variables in Eqs. (7)–(11) are defined as follows: k is the turbulent kinetic energy (m^2/s^2); ω is the specific dissipation rate (1/s); P_k is the term for turbulence production; β, β^*, α, σ_k, σ_ω, and $\sigma_{\omega 2}$ are model constants; μ is the laminar dynamic viscosity (kg/(m·s)); μ_t is the turbulent viscosity; F_1 and F_2 are the blending functions used in the SST formulation.

2.3. Reactive species transport

Reactive transport in this study involves non-conservative chemical species whose concentrations change not only through advection and diffusion but also through chemical transformation. A non-conservative species may be generated or depleted depending on the reaction pathways in which it participates, making it essential to solve the reactive species transport equations simultaneously with the flow field. The transport of chemical species in airflow for non-conservative species can be expressed as follows:

$$\frac{\partial(\rho Y_i)}{\partial t} + \nabla\cdot(\rho u Y_i) = -\nabla\cdot J_i + R_i + S_i \tag{12}$$

In Eq. (12), $\rho u Y_i$ represents the advection term, J_i denotes the diffusion term, R_i is the chemical reaction term, and S_i is the additional pollutant source term. The terms J_i and R_i are defined as follows:

$$J_i = -\left(\frac{\mu}{Sc} + \frac{\mu_t}{Sc_t}\right) \nabla Y_i \tag{13}$$

$$R_i = \nu_i M_i k_r(T) \prod_j C_j^{\nu_j} \tag{14}$$

The temperature-dependent reaction rate constant $k_r(T)$ is calculated using the Arrhenius equation:

$$k_r(T) = AT^n \exp\left(-\frac{E_a}{RT}\right) \tag{15}$$

In the non-conservative gas equation, the following assumptions are applied:

- Steady-state condition:

$$\frac{\partial(\rho Y_i)}{\partial t} = 0 \tag{16}$$

- Assuming steady-state conditions and a predominantly one-dimensional flow along the streamwise (x) direction, with constant density (ρ) and velocity (u), the convective transport term can be simplified as:

$$\nabla \cdot (\rho u Y_i) = \rho u \frac{dY}{dx} \tag{17}$$

Substituting this expression into Eq. (12) yields the reduced one-dimensional form of the species transport equation:

$$\rho u \frac{dY}{dx} = \frac{d}{dx}\left[\left(\frac{\mu}{Sc} + \frac{\mu_t}{Sc_t}\right)\frac{dY}{dx}\right] + R_i + S_i \tag{18}$$

If μ, μ_t, Sc, and Sc_t are assumed constant along x, Eq. (18) simplifies to

$$\rho u \frac{dY}{dx} = \left(\frac{\mu}{Sc} + \frac{\mu_t}{Sc_t}\right)\frac{d^2Y}{dx^2} + R_i + S_i \tag{19}$$

Then, the effective diffusion coefficient (D_{eff}) is defined as follows:

$$D_{\text{eff}} = \frac{1}{\rho}\left(\frac{\mu}{Sc} + \frac{\mu_t}{Sc_t}\right) \tag{20}$$

If the pollutant concentration is defined as $C = \rho Y$, then

$$u\frac{dC}{dx} = D_{\text{eff}}\frac{d^2C}{dx^2} + R_i + S_i \tag{21}$$

The additional variables in Eqs. (20) and (21) are defined as follows: S_i denotes other pollutant sources within the volume; Sc is the laminar Schmidt number; Sc_t is the turbulent Schmidt number; k_r is the reaction rate constant based on the Arrhenius equation; A is the pre-exponential factor or reaction kinetic constant; T is the temperature; E_a is the activation energy (J/mol or J/kmol); R is the ideal gas constant; C is the species concentration expressed in solver-consistent units (kmol/m^3), while the reported concentrations are converted to μg/m^3 for comparison with observed ambient concentrations; and Y is the mass fraction of the pollutant.

The reactive transformation of NO_2 and O_3 in the street canyon is represented by the following reactions:

$$\text{NO}_2 + h\nu \rightarrow \text{NO} + \text{O} \tag{22}$$

$$\mathrm{O} + \mathrm{O_2} + M \rightarrow \mathrm{O_3} + M \tag{23}$$

$$\mathrm{NO} + \mathrm{O_3} \rightarrow \mathrm{NO_2} + \mathrm{O_2} \tag{24}$$

Reaction (22) is governed by the photolysis frequency:

$$R_1 = J[\mathrm{NO_2}] \tag{25}$$

In this study, the photolysis frequency J is treated as a prescribed constant representative of daytime tropical conditions, rather than being derived from an attenuation-based formulation. The use of a constant photolysis frequency in the present study was adopted to isolate the first-order effect of obstacle-induced flow modification on reactive pollutant transport while keeping the chemical mechanism computationally tractable. Although the actual photolysis rate varies with solar angle, cloud cover, and atmospheric composition throughout the day, incorporating such temporal variability would require a more comprehensive radiative-photochemical framework beyond the scope of the present steady-state CFD analysis. The value of J is specified as $0.005\ \mathrm{s}^{-1}$ based on literature-reported ranges for similar environmental conditions [32, 33]. This assumption provides a simplified representation of photochemical processes and avoids the need for detailed radiative transfer modeling. In reality, J depends on actinic flux, solar angle, and atmospheric conditions; however, such effects are beyond the scope of the present study.

Homogeneous gas-phase reactions, i.e., Eqs. (23) and (24), are modeled using literature-based reaction-rate constants [35].

$$R_n = AT^n \exp\left(-\frac{E_a}{RT}\right) \tag{26}$$

where R_n is the reaction rate (kmol/m^3·s), A is the pre-exponential factor, T is the temperature (K), n is the temperature exponent, E_a is the activation energy (J/kmol), and R is the universal gas constant. Reaction (23) is a three-body reaction whose effective rate constant is expressed as

$$k_{\mathrm{eff}} = k_0[M] \tag{27}$$

with:

$$k_0(300\,\mathrm{K}) = 6.0 \times 10^{-34}\ \mathrm{cm^6\,molecule^{-2}\,s^{-1}} \tag{28}$$

At 1 atm and 298 K, the concentration of air is

$$[M] = 2.46 \times 10^{19}\ \mathrm{molecule/cm^3} \tag{29}$$

Thus, the effective rate constant becomes

$$k_{\mathrm{eff}} = 6.0 \times 10^{-34}\ \frac{\mathrm{cm^6}}{\mathrm{molecule^2 \cdot s}} \times 2.46 \times 10^{19}\ \frac{\mathrm{molecule}}{\mathrm{cm^3}} = 1.476 \times 10^{-14}\ \frac{\mathrm{cm^3}}{\mathrm{molecule \cdot s}} \tag{30}$$

To be compatible with ANSYS Fluent, this rate constant was converted into m^3/kmol·s using Avogadro's number:

$$k_2 = k_{\mathrm{eff}} \times N_A \tag{31}$$

$$k_2 = 1.476 \times 10^{-14}\ \frac{\mathrm{cm^3}}{\mathrm{molecule \cdot s}} \times 10^{-6}\ \frac{\mathrm{m^3}}{\mathrm{cm^3}} \times 6.022 \times 10^{26}\ \frac{\mathrm{molecule}}{\mathrm{kmol}} \tag{32}$$

$$k_2 = 8.89 \times 10^{6}\ \frac{\mathrm{m^3}}{\mathrm{kmol \cdot s}} \tag{33}$$

The reaction between NO and O_3 (Reaction (24)) has a temperature-dependent rate constant:

$$k_{\mathrm{NO+O_3}}(298\,\mathrm{K}) = 1.8 \times 10^{-14}\ \mathrm{cm^3\,molecule^{-1}\,s^{-1}} \tag{34}$$

Converted to the Fluent convention:

$$k_3 = k_{\mathrm{NO+O_3}}(298\,\mathrm{K}) \times N_A \tag{35}$$

$$k_3 = 1.8 \times 10^{-14}\ \frac{\mathrm{cm}^3}{\mathrm{molecule \cdot s}} \times 10^{-6}\ \frac{\mathrm{m}^3}{\mathrm{cm}^3} \times 6.022 \times 10^{26}\ \frac{\mathrm{molecule}}{\mathrm{kmol}} \tag{36}$$

$$k_3 = 1.08 \times 10^{7}\ \frac{\mathrm{m}^3}{\mathrm{kmol \cdot s}} \approx 1.1 \times 10^{7}\ \frac{\mathrm{m}^3}{\mathrm{kmol \cdot s}} \tag{37}$$

For clarity, the simplified chemical mechanism adopted in this study, together with the corresponding rate parameters and literature sources, is summarized in Table 1.

Table 1. Summary of the simplified chemical mechanism and reaction parameters used in the CFD model

Reaction	Expression	Rate parameter	Value / Unit	Source / Note
R1	$NO_2 + h\nu \rightarrow NO + O$	J	0.005 s^{-1}	Prescribed constant representative of daytime tropical conditions; literature-based [32, 33]
R2	$O + O_2 + M \rightarrow O_3 + M$	k_2	8.89×10^6 m^3/(kmol·s)	Derived from effective three-body reaction rate and converted to Fluent-compatible units [31, 35]
R3	$NO + O_3 \rightarrow NO_2 + O_2$	k_3	1.1×10^7 m^3/(kmol·s)	Literature-based rate constant converted to Fluent-compatible units [31, 35]

The adopted reaction-rate constants provide a simplified representation of the coupled NO_2–O_3 chemical system considered in this study [36]. In CFD simulations using ANSYS Fluent, the input data for NO_2 and O_3 concentrations must be expressed in the form of mass fractions or mole fractions of pollutant species. In this context, species refer to chemical components present in the gas mixture. The mass fraction values were specified in the species boundary condition settings. In this study, the chemical species considered were NO_2, O_3, N_2, O_2, H_2O, O, and NO.

The background concentrations obtained from field measurements were originally expressed in μg/m^3. Prior to implementation in the CFD model, these values were converted into molar concentrations (kmol/m^3) using the molecular weight of each species and subsequently transformed into species fractions consistent with the species transport formulation in ANSYS Fluent. This procedure ensures consistency between the imposed inlet conditions and the reaction-rate constants, which are defined in kmol-based units.

2.4. Mesh Generation and Quality

In CFD simulations, mesh quality is a crucial factor in ensuring the accuracy and reliability of the results. A well-constructed mesh enables accurate resolution of airflow and pollutant transport, whereas poor mesh quality may introduce numerical errors and reduce the accuracy of the simulation. In this study, a high-quality computational mesh was generated to simulate the airflow and reactive pollutant transport within the street canyon.

The mesh consists of 25,162,079 elements, providing fine spatial resolution, particularly in critical regions such as near the urban obstacles (buildings and vegetation) and the ground surface (Table 2). Several mesh quality indicators were evaluated, including skewness, aspect ratio, and orthogonal quality. The minimum, maximum, and average skewness values were 1.3057×10^{-10}, 0.79993, and 0.17569, respectively, with a standard deviation of 0.12421. For the aspect ratio, the minimum, maximum, and average values were 1.0, 97.774, and 4.837, respectively, with a standard deviation of 9.1106. In addition, the orthogonal quality ranged from 0.20007 to 1.0, with an average value of 0.82318 and a standard deviation of 0.12307. These values indicate that the generated mesh is of acceptable quality for CFD simulation of airflow and reactive pollutant transport in the street canyon.

The skewness of the mesh elements, which measures the deviation from ideal element shapes, shows a minimum value of 1.3057×10^{-10}, a maximum value of 0.79993, and an average value of 0.17569. This relatively low

Table 2. Mesh Quality

No	Parameter	Number
1	Elements	25,162,079
2	Skewness min	1.3057×10^{-10}
3	Skewness max	0.79993
4	Skewness ave	0.17569
5	Std dev skewness	0.12421
6	Aspect ratio min	1.0
7	Aspect ratio max	97.774
8	Aspect ratio ave	4.837
9	Std dev aspect ratio	9.1106
10	Ortho quality min	0.20007
11	Ortho quality max	1.0
12	Ortho quality ave	0.82318
13	Std dev ortho quality	0.12307

average skewness indicates that most mesh elements are close to their ideal shapes, thereby supporting accurate numerical calculations. The standard deviation of 0.12421 further confirms that the mesh is generally well constructed, with only a limited number of highly skewed elements.

The orthogonal quality of the mesh, which indicates how close the mesh elements are to being orthogonal, is another important indicator of mesh quality. In this study, the minimum orthogonal quality is 0.20007, the maximum orthogonal quality is 1.0, and the average orthogonal quality is 0.82318. The standard deviation of 0.12307 indicates that the mesh is predominantly composed of well-orthogonal elements, which is essential for accurate flow and turbulence predictions. Although the maximum aspect ratio reaches 97.774, this value does not represent the general condition of the mesh. The relatively low average aspect ratio (4.837), together with the low average skewness and good average orthogonal quality, indicates that the mesh quality remains acceptable for the present CFD simulation. Therefore, the high aspect-ratio value should be understood as a localized mesh feature rather than a dominant property of the computational grid as a whole.

Overall, the mesh quality assessment confirms that the generated mesh is sufficiently good for simulating airflow and pollutant dispersion in the street canyon. Although some elements exhibit relatively high aspect ratios, the overall mesh quality, as indicated by the low skewness and good orthogonal quality, ensures the reliability of the simulation results. Therefore, the generated mesh is considered suitable for CFD analysis of reactive pollutant transport in the urban environment.

2.5. Boundary conditions

Appropriate boundary conditions are essential to ensure that the simulated airflow and reactive pollutant transport realistically represent the physical conditions of the urban street canyon. In this study, the boundary conditions were defined based on measured meteorological parameters, street geometry, and pollutant concentrations representative of tropical urban environments. The upstream boundary of the computational domain was prescribed as a velocity inlet, representing the approaching atmospheric flow during the rainy-season condition. The mean wind speed at pedestrian level was set to 0.38 m/s, consistent with local meteorological observations. Turbulence quantities were specified using a turbulence intensity of 5% and a turbulent viscosity ratio of 10, corresponding to moderately unstable tropical urban conditions. The thermal boundary condition was set to 28.51°C, reflecting typical ambient temperatures in Surabaya during the study period. Species mass fractions at the inlet were assigned according to the observed background concentrations of NO_2 and O_3, expressed in mass-fraction form for consistency with the species transport framework. Table 3 summarizes the boundary conditions applied in the CFD simulation, including the boundary types, prescribed parameters, and their physical roles in representing the urban street canyon environment. These values were obtained by converting measured concentrations from μg/m^3 into molar concentrations and subsequently into species fractions compatible with the solver.

Table 3. Boundary conditions used in the CFD simulation

Boundary/Zone	Type	Specification	Remarks
Inlet	Velocity inlet	Wind speed = 0.38 m/s; temperature = 28.51°C; turbulence intensity = 5%; turbulent viscosity ratio = 10	Represents approaching rainy-season airflow
Top boundary	Symmetry	Zero normal gradients of velocity, temperature, and species concentrations	Represents undisturbed atmosphere above the canyon
Side boundaries	Symmetry	Zero normal gradients of velocity, temperature, and species concentrations	Assumes negligible lateral influence at domain edges
Building facades	Wall	No-slip wall	Resolves wall shear and recirculation effects
Road surface	Wall + source region	No-slip wall; constant NO and NO_2 source terms imposed volumetrically in near-surface cells	Represents traffic-related emissions
Simplified roadside obstacle regions	Wall	No-slip wall	Represents simplified solid-barrier effects under the present modeling assumptions
Species inlet	Species specification	Background NO_2 and O_3 concentrations specified as mass fractions	Consistent with species transport model

The upper boundary of the domain was treated as a symmetry boundary, implying zero normal gradients of velocity, temperature, and species concentrations. This condition is commonly applied in urban-scale CFD studies to represent an undisturbed atmosphere above the influence height of street-level turbulence. The symmetry assumption avoids artificial shear or momentum fluxes at the top boundary and reduces computational cost while maintaining physical consistency for the simulated flow regime. The vertical extent of the domain was set to 60 m, corresponding to a domain height-to-building-height ratio of $L_z/H = 60/15 = 4$, which is within the range commonly adopted in RANS-based urban street canyon simulations [26]. The left and right boundaries of the computational domain were also assigned symmetry boundary conditions, representing flow conditions sufficiently far from canyon-induced disturbances. The lateral extent of the domain was set to 124 m, yielding a lateral-to-building-height ratio of $L_y/H = 124/15 \approx 8.3$. According to the best-practice guidelines of Franke et al. [26], a minimum lateral clearance of $5H$ on each side of the obstacle array is generally recommended to ensure that lateral boundary effects do not contaminate the flow field within the region of interest. In the present configuration, the total width of the canyon array, including the two building rows and the intervening roadway and obstacle strips, is approximately 84 m. The remaining lateral clearance of approximately 20 m on each side corresponds to a ratio of approximately $1.3H$ per side. Although this is smaller than the recommended $5H$ per-side clearance, the symmetry boundary condition was selected over an inlet-type lateral boundary because the dominant flow direction in the present configuration is streamwise, and the lateral velocity gradients are expected to be small at these boundary planes. Furthermore, the use of symmetry boundaries rather than periodic boundaries is consistent with the assumption of an isolated idealized canyon segment [17]. This symmetry-boundary treatment represents an idealized street-canyon segment and does not explicitly account for lateral inflow, cross-street interactions, or intersection-induced disturbances. These effects remain a limitation of the present CFD framework. This approach assumes that the lateral extent of the domain is large enough such that velocity and scalar gradients normal to these boundaries are negligible. The use of symmetry boundaries reduces unnecessary computational cost while preventing reflections or distortions of the flow and species fields near the lateral edges of the domain.

All building facades, road surfaces, and simplified roadside obstacle regions were treated as no-slip walls, where the tangential velocity components vanish. In the present model, the roadside green strips are represented as simplified solid obstacles rather than porous vegetation canopies. Therefore, the simulation does not resolve canopy drag, sub-canopy turbulence production, or pollutant deposition on leaf surfaces. The results should thus be interpreted as the effect of obstacle presence under a solid-barrier assumption, rather than as a fully realistic representation of vegetation aerodynamics. Species mass flux at solid surfaces was set to zero, except for the street surfaces where constant emission source terms of NO and NO_2 were applied to represent traffic-related pollutant release. These source terms were imposed volumetrically within the near-surface fluid cells rather than as boundary fluxes, thereby ensuring numerical stability and compatibility with Fluent's species transport solver. The NO and NO_2 emission rates used in the simulation were calculated based on the number of vehicles passing through the study area multiplied by the corresponding emission factors. The vehicle count data were obtained from the Surabaya City Transportation Agency, while the emission factors were adopted from the Indonesian Minister of Environment Regulation No. 12 of 2010 concerning the implementation of regional air pollution control. These factors were used to estimate the emissions produced by each vehicle category operating on the studied roadway. In the present study, tropical conditions are represented through rainy-season meteorological inputs, ambient temperature, and a prescribed photolysis rate characteristic of daytime tropical conditions. Nevertheless, buoyancy effects associated with temperature gradients, as well as the influence of humidity on reactive transport, were not evaluated in detail. Thus, the current CFD framework should be regarded as weakly coupled with respect to thermal-buoyancy effects, and the results are interpreted primarily from the perspective of obstacle-modified airflow and simplified chemistry.

3. Results and Discussion

3.1. Static Pressure Distribution

The static pressure contours obtained from the k–ω SST model (Fig. 4) show distinct differences between the obstacle and non-obstacle configurations, revealing the influence of urban obstacle elements (including simplified roadside obstacle regions) on the aerodynamic environment of the street canyon. In both scenarios, the highest pressures occur on the windward-facing facades, where the incoming flow impinges directly on the building surfaces. This pressure buildup is consistent with classical bluff-body aerodynamics, in which stagnation zones develop at the upstream faces of obstacles. Such behavior is commonly observed in street canyon configurations, where building facades act as bluff bodies and induce flow separation and pressure gradients near the surfaces. However, the magnitude and spatial extent of the high-pressure region differ noticeably between the two configurations.

In the with-obstacle case (Fig. 4a), the presence of simplified roadside obstacle regions and geometric irregularities generates additional localized stagnation points along the windward facade. These solid obstacle elements modify the effective flow passage and induce local flow deceleration, resulting in a broader high-pressure band. Elevated pressure is also observed near the upstream corners and upper edges of the canyon, where the approaching flow separates and forms shear layers that propagate downstream. In contrast, the internal region of the canyon exhibits relatively lower and more spatially variable pressures, indicating the formation of recirculation cells and weak ventilation zones caused by the interaction between buildings and solid obstacle strips. Under the present modeling assumption, these obstacle regions act as flow-blocking elements that disrupt airflow and promote localized recirculation, rather than representing the detailed aerodynamic behavior of porous vegetation canopies.

In contrast, the without-obstacle configuration shown in Fig. 4 (panel b) displays a smoother and more symmetric pressure field along the windward facade. The absence of internal obstacle elements reduces localized flow obstruction, allowing the incoming airstream to interact more uniformly with the building face. As a result, a more coherent stagnation zone is formed, accompanied by a cleaner transition from high pressure at the windward wall to lower pressure toward the canyon interior. The reduced surface roughness also diminishes pressure perturbations near the canyon roofline, suggesting a more stable shear layer with less fragmentation [37].

Across both scenarios, the leeward facades exhibit substantially lower pressures, which are associated with flow separation and wake formation. These low-pressure zones are more pronounced and spatially extensive in the obstacle case, indicating stronger recirculation and less efficient pressure recovery behind the buildings. This behavior reflects the influence of solid obstacle-induced flow blockage in enhancing wake turbulence and disrupting momentum exchange within the canyon [9, 38].

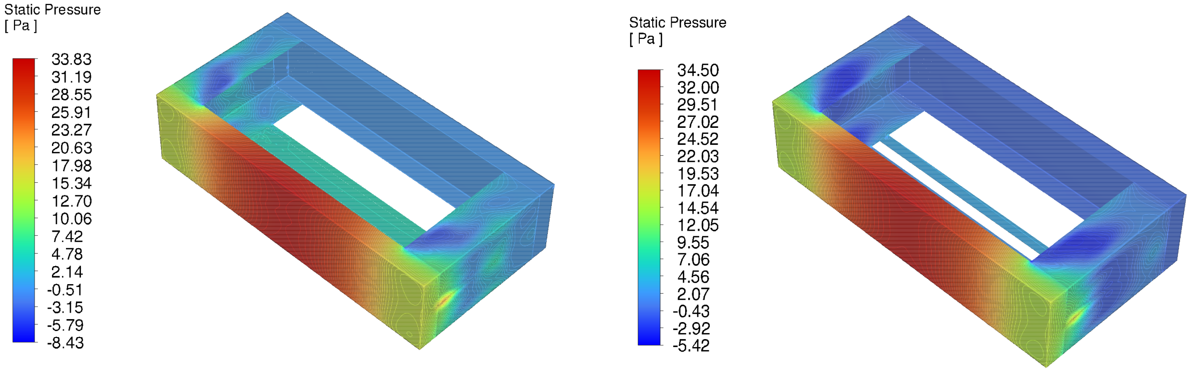

(a) With obstacle

(b) Without obstacle

Figure 4. Static pressure contours (Pa) predicted by the k–ω SST model for (a) with obstacle and (b) without obstacle configurations

A comparison of the static pressure values predicted by the k–ω SST model, both with and without obstacles, for each zone is presented in Table 4. The zone-averaged static pressure values are consistent with the contour patterns discussed in Section 3.1 and provide a quantitative measure of how obstacles modify the pressure field within the canyon. At the inlet, the average static pressure is similar in both configurations, namely 23.30 Pa for the obstacle case and 23.95 Pa for the non-obstacle case, reflecting the imposed upstream boundary conditions. However, clear differences emerge within the canyon interior. The pressure values in Street 1 and Street 2 are substantially higher in the obstacle configuration, with Street 1 exhibiting an average pressure of 5.09 Pa compared with 3.67 Pa in the non-obstacle case. This increase is associated with localized stagnation zones near the building facades and simplified obstacle regions, which impede airflow and increase resistance to flow penetration. The elevated street-level pressure therefore indicates stronger resistance to incoming flow and is consistent with the presence of localized stagnation and shear layers induced by solid obstacle effects [39]. It should be emphasized that these effects arise from the solid-barrier representation adopted in the present model, and do not explicitly account for canopy-scale turbulence or permeability effects associated with real vegetation.

Table 4. Average static pressure results in each zone

No	Zone	Average Static Pressure [Pa]	
		With obstacle	***Without obstacle***
1	*Building 1*	0.00	-
2	*Building 2*	0.00	-
3	*Green space 1*	5.19	-
4	*Green space 2*	4.92	-
5	*Green space 3*	4.18	-
6	Inlet	23.30	23.95
7	Outlet	0.49	0.49
8	*Street 1*	5.09	3.67
9	*Street 2*	4.50	2.31
10	*Top air volume*	2.16	2.25
11	*Wall left domain*	0.56	0.40
12	*Wall right domain*	0.55	0.41
	Net	3.60	3.69

The green-space regions show intermediate pressure levels (4.18–5.19 Pa), which are lower than the inlet pressure but higher than the outlet pressure, confirming their role as transition regions where the external flow decelerates and partially redistributes before entering the canyon core [18]. The top-air volume exhibits relatively low mean pressures, approximately 2.2 Pa in both configurations, indicating the dominance of the external free stream and the absence of strong stagnation above roof level. The lateral boundaries, namely the left and right domain walls, remain close to atmospheric pressure, with slightly higher values in the obstacle configuration (0.55–0.56 Pa) than in the non-obstacle configuration (0.40–0.41 Pa), reflecting weak but noticeable blockage effects. The domain-averaged ("Net") pressure is nearly identical in both simulations, with values of 3.60 and 3.69 Pa, confirming that obstacles primarily redistribute pressure locally rather than substantially altering the global pressure balance of the system.

Overall, the pressure contours demonstrate that the inclusion of urban obstacles intensifies spatial pressure gradients, promotes additional stagnation sub-regions, and amplifies wake-induced low-pressure zones. These modifications directly affect the strength of flow recirculation and the air-exchange processes within the canyon, with important implications for pollutant retention and ventilation efficiency under tropical urban conditions.

3.2. *Airflow velocity distribution*

The velocity magnitude contours generated using the k–ω SST model (Fig. 5) reveal the substantial influence of urban obstacles on airflow dynamics within the street canyon. In both configurations, the incoming wind accelerates around the windward corners of the buildings, producing zones of elevated velocity due to flow constriction and shear generation. However, the internal flow structures and ventilation patterns differ markedly between the obstacle and non-obstacle cases.

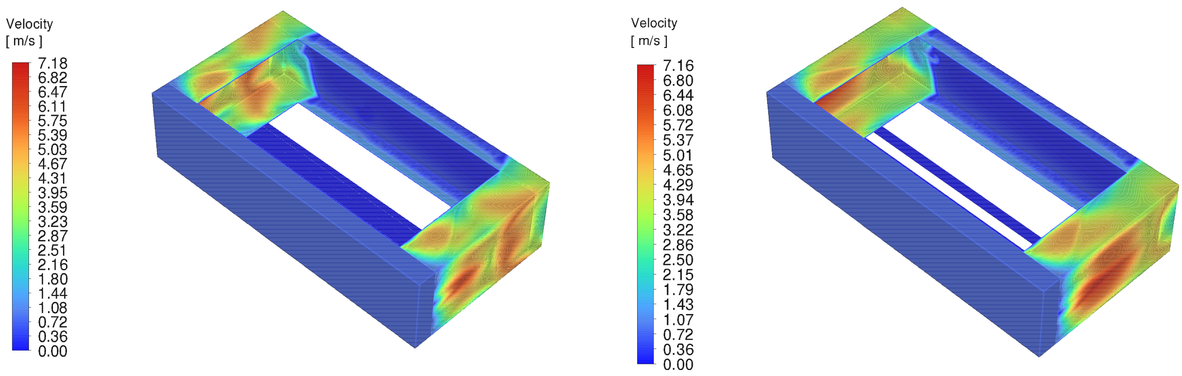

(a) With obstacle (b) Without obstacle

Figure 5. Velocity contours (m/s) predicted by the k–ω SST model for (a) with obstacle and (b) without obstacle configurations

In the with-obstacle configuration shown in Fig. 5 (panel a), the presence of simplified roadside obstacle regions and internal geometric variations induces stronger flow disruption at the canyon entrance. High-velocity regions are concentrated along the upper windward edges, where the incoming stream separates from the roofline and forms a shear layer that extends downstream. Behind this shear layer, the velocity within the canyon interior decreases significantly, creating a broad low-speed zone. This weakened ventilation region corresponds to the recirculation cell typically observed in street canyon flows. Under the present solid-obstacle representation, these regions act as flow-blocking elements that reduce the effective flow cross-sectional area, thereby modifying the structure and strength of the recirculation cell. It is important to emphasize that, in this model, the obstacle regions are treated as solid barriers rather than porous vegetation canopies. Therefore, the observed reduction in ventilation is associated with flow obstruction and recirculation modification, rather than canopy drag or sub-grid turbulence generation mechanisms [39, 40].

In contrast, the without-obstacle configuration shown in Fig. 5 (panel b) displays more efficient wind penetration into the canyon. The shear layer formed at roof level is smoother and more coherent, allowing a clearer dominant vortex to develop within the canyon. Higher velocities are observed near the leeward wall, indicating a stronger primary recirculation structure. The absence of internal obstacle elements allows a more continuous flow pathway, facilitating more effective momentum transfer from the free stream into the canyon. Consequently, the velocity deficit in the canyon core is smaller, and the overall airflow appears more organized and energetic than in the obstacle case.

Furthermore, a comparison of the airflow velocity predicted by the k–ω SST model, with and without obstacles in each zone, is presented in Table 5. The zone-averaged velocity magnitudes further clarify how the obstacles redistribute local airflow within the canyon and modify the overall flow structure. At the inlet and outlet, the mean velocities are nearly identical in both configurations, namely 1.94 and 1.92 m/s at the inlet and 0.92 m/s at the outlet, reflecting the consistency of the imposed external forcing. The apparent difference between the 0.38 m/s value given in the boundary-condition specification and the 1.94 m/s value reported in Table 5 arises because they represent different quantities. The former denotes the prescribed reference wind speed at pedestrian level used to define the inlet condition, whereas the latter denotes the zone-averaged velocity magnitude obtained from the CFD field in the inlet region. Accordingly, the two values should not be compared as identical measures of inlet flow speed. In contrast, substantial differences occur at street level. The average velocities in Street 1 and Street 2 are markedly higher in the obstacle configuration (0.35 and 0.50 m/s) compared with the non-obstacle case (0.06 and 0.08 m/s). At first glance, this result may appear counter-intuitive, as obstacles are generally expected to impede airflow. However, this behavior can be explained by the flow-constriction effect induced by the simplified solid-obstacle representation used in the present model. The presence of these obstacles reduces the effective flow cross-sectional area, leading to localized acceleration of airflow in the remaining open regions, similar to a channeling or guide-vane effect [5, 41]. Consequently, higher velocities are observed in confined passages between obstacles, even though the overall flow field exhibits reduced ventilation efficiency.

Table 5. Average airflow velocity results in each zone

No	Zone	Average velocity magnitude (m/s)	
		With obstacle	*Without obstacle*
1	*Building 1*	0.00	-
2	*Building 2*	0.00	-
3	*Green space 1*	0.34	-
4	*Green space 2*	0.18	-
5	*Green space 3*	0.27	-
6	Inlet	1.94	1.92
7	Outlet	0.92	0.92
8	*Street 1*	0.35	0.06
9	*Street 2*	0.50	0.08
10	*Top air volume*	0.0042	0.0038
11	*Wall left domain*	3.14	3.09
12	*Wall right domain*	3.12	3.09
	Net	0.65	0.64

It is important to distinguish between local velocity magnitudes and overall ventilation efficiency. While localized velocities increase in certain regions, the overall airflow structure becomes more fragmented, with disrupted recirculation patterns and reduced effective air exchange between the canyon interior and the overlying atmosphere. This behavior is directly influenced by the modeling assumption in which roadside vegetation is represented as solid obstacles. Under this assumption, the obstacles act as impermeable barriers that redirect and constrict the flow, rather than as porous media that would dissipate momentum through drag and turbulence. Therefore, the observed velocity increase should be interpreted as a consequence of the simplified solid-obstacle representation rather than as a realistic depiction of vegetative aerodynamic effects. Thus, although obstacles increase local velocity magnitudes in restricted regions, they simultaneously reduce the overall ventilation performance of the canyon, resolving the apparent contradiction between higher velocities and reduced air-exchange rates [37, 42].

The green-space regions exhibit low but non-negligible velocities, ranging from 0.18 to 0.34 m/s, indicating that these zones act as partially sheltered corridors where air motion is reduced but still sufficient to sustain mixing between the main flow and the canyon interior. The very low velocities observed in the top-air volume, 0.0042 m/s with obstacles and 0.0038 m/s without obstacles, are consistent with restricted air movement near roof level. This finding indicates that urban obstacles affect not only near-ground airflow but also ventilation efficiency at higher elevations, which is important for pollutant exchange at the canopy level. Conversely, the lateral walls show the highest mean velocities, approximately 3.1 m/s in both configurations, because they are directly exposed to the approaching flow and channel the main stream around the building array. The domain-averaged net velocity remains nearly unchanged, with values of 0.65 and 0.64 m/s, reinforcing the conclusion that obstacles mainly reorganize the internal flow structure rather than substantially modifying the large-scale momentum budget.

Overall, the velocity contours demonstrate that urban obstacles substantially alter the canyon ventilation regime by redistributing flow pathways, inducing localized accelerations, and modifying recirculation structures [40, 43], rather than uniformly enhancing airflow. Such modifications have direct implications for the spatial distribution and chemical transformation of reactive pollutants within the tropical urban street canyon. It should be noted that more explicit ventilation metrics, such as Air Change per Hour (ACH) or Purge Flow Rate, were not evaluated in the present study. Future work should incorporate such metrics to provide a more quantitative assessment of ventilation efficiency in obstacle-influenced street canyons.

3.3. Distribution of NO_2 and O_3 Concentrations

The concentration of reactive pollutants in the simulated street canyon reflects the combined effects of emission strength, airflow dynamics, and photochemical transformations occurring within the computational domain. For clarity and consistency with ambient air quality measurements, the concentration values presented in this section are reported in μg/m^3, whereas the CFD solver internally operates using species fractions derived from molar concentrations. It should be noted that this study is not intended to provide a comprehensive prediction of urban ozone chemistry. Instead, the simplified NO_x–O_3 mechanism was adopted to capture the first-order influence of obstacle-modified airflow on reactive pollutant transport within the street canyon. In this study, NO and NO_2 emissions were released at street level as constant source terms, while the background concentrations of NO_2, O_3, and ambient air were imposed at the inlet boundary in the form of mass fractions. The coupled transport–reaction mechanism enables the model to simulate species movement through advective and diffusive processes while simultaneously accounting for chemical reactions such as NO_2 photolysis and O_3 titration. By tracking the concentrations of NO_2 and O_3 in each zone, the model provides a more comprehensive representation of pollutant dynamics within the street canyon. Table 6 presents the spatially averaged concentrations of NO_2 and O_3 in each zone for both configurations. It should be emphasized that the values reported represent spatially averaged concentrations over each computational zone, and therefore they should not be interpreted as point-scale observations or local maximum concentrations within the canyon.

Several important observations emerge from the results presented in Table 6. In the obstacle configuration, NO_2 concentrations reach 9.21 μg/m^3 in Street 1 and 8.04 μg/m^3 in Street 2, which are substantially higher than those in the non-obstacle configuration, where the corresponding values decrease to 0.38 and 0.60 μg/m^3, respectively. This marked difference indicates that the presence of obstacles significantly suppresses ventilation efficiency and promotes pollutant accumulation within the canyon [42, 44]. This accumulation is primarily associated with reduced effective air exchange and increased residence time, rather than solely with local emission intensity. For O_3, the obstacle case yields concentrations ranging from 2.99 to 5.72 μg/m^3, whereas the non-obstacle configuration produces only 1.03 to 1.62 μg/m^3. This behavior should not be interpreted as a direct consequence of increased NO_2 concentration alone. Instead, the O_3 distribution reflects the balance between competing chemical processes, namely photochemical production via NO_2 photolysis and chemical loss through NO-induced titration [46]. In urban environments, NO can rapidly react with O_3 and reduce its concentration, meaning that elevated NO_2 levels do not necessarily correspond to increased O_3 formation. The observed increase in O_3 concentration under

Table 6. Results of the average concentration of NO_2 and O_3 in each zone

No	Zone	With obstacle		Without obstacle	
		C NO_2 (μg/m^3)	C O_3 (μg/m^3)	C NO_2 (μg/m^3)	C O_3 (μg/m^3)
1	*Building 1*	0	0	-	-
2	*Building 2*	0	0	-	-
3	*Green space 1*	0.22	0.03	-	-
4	*Green space 2*	1.03	2.53	-	-
5	*Green space 3*	1.94	5.25	-	-
6	Inlet	18.53	50.21	18.53	50.22
7	Outlet	16.54	44.79	17.61	47.68
8	*Street 1*	9.21	2.99	0.38	1.03
9	*Street 2*	8.04	5.72	0.60	1.62
10	*Top air volume*	1.26E-39	7.95E-38	3.45E-40	2.17E-38
11	*Wall left domain*	16.32	44.22	17.09	46.31
12	*Wall right domain*	16.26	44.06	17.09	46.32
	Net	5.08	13.74	5.28	14.31

the obstacle configuration suggests that obstacle-induced flow modification alters the balance between transport and chemical reaction. In particular, increased residence time within recirculation zones allows air parcels to undergo more extensive photochemical processing, thereby enabling O_3 production pathways to compete more effectively with titration losses. From a transport–reaction perspective, this behavior can be interpreted in terms of the relative timescales of advection and chemical transformation, where longer residence times enhance the influence of reaction kinetics on local concentration fields [36].

In the obstacle configuration, the three green-space zones show increasing pollutant levels from the outer strip toward the central strip. This gradient reflects flow deceleration and recirculation induced by the simplified solid obstacle regions, rather than detailed canopy-scale vegetation effects [45]. Green space 3, located deeper within the canyon and closer to the pollutant source, tends to retain pollutants more effectively due to reduced momentum transfer and weaker interaction with the free-stream flow. In contrast, Green space 1, positioned at the outermost lateral boundary of the canyon domain, is more directly exposed to the approaching free-stream flow. Its peripheral location allows greater momentum exchange with the incoming airstream, resulting in more efficient local ventilation and, consequently, substantially lower spatially averaged concentrations of both NO_2 (0.22 μg/m^3) and O_3 (0.03 μg/m^3) compared with Green space 2 and Green space 3. The markedly lower O_3 concentration in Green space 1 relative to the inner zones further suggests that NO-mediated titration is more active in this region, where fresher traffic emissions interact with the background O_3 before significant photochemical processing can occur. These spatial differences among the green-space zones therefore reflect the interplay between the local flow field, pollutant residence time, and the simplified solid-obstacle representation adopted in the present model, rather than vegetation-specific aerodynamic or deposition effects. Under the present modeling assumption, these regions act as flow-blocking elements that promote localized stagnation and pollutant retention, which in turn increases the effective residence time available for chemical transformation.

As a result, the local O_3 concentration represents a dynamic balance between photochemical production and NO-mediated destruction, rather than a simple accumulation process. It should be emphasized that the current chemical mechanism is highly simplified and includes only NO_x–O_3 interactions without the inclusion of volatile organic compounds (VOCs). In real urban atmospheres, VOCs play a critical role in controlling ozone formation regimes (NO_x-limited or VOC-limited), and their omission represents a significant limitation of the present model [46, 47]. As a consequence, the model may not fully capture the sensitivity of ozone formation to precursor composition and may place greater emphasis on NO_2 photolysis pathways. Therefore, the predicted O_3 concentrations should be interpreted with caution as a simplified representation of urban photochemical processes rather than a fully comprehensive chemical mechanism.

At the inlet, both configurations exhibit nearly identical concentrations, with NO_2 = 18.53 μg/m^3 and O_3 = 50.21–50.22 μg/m^3, as prescribed by the boundary condition. However, substantial differences develop inside the canyon, highlighting the influence of internal geometry and obstacles on airflow restriction and pollutant redistribution. These differences are particularly evident in the recirculation regions behind the buildings. The outlet concentrations also differ despite identical inflow conditions. The lower outlet concentrations in the obstacle case indicate that pollutant removal from the canyon is less efficient, consistent with reduced ventilation and enhanced internal recirculation [46]. As expected, concentrations in the top-air volume are extremely low in both scenarios, confirming that most chemical interaction and pollutant retention occur near street level. The slightly higher values in the obstacle case, on the order of 10^{-38} to 10^{-39} μg/m^3, reflect a modest upward transport of reaction products, although these remain negligible compared with ground-level concentrations. These results are consistent with the velocity and pressure patterns discussed in Sections 3.1 and 3.2, demonstrating that solid obstacle-induced flow modification is a key determinant of reactive pollutant behavior in tropical street canyons. Overall, the results highlight the strong coupling between flow dynamics and chemical transformation, where obstacle-induced changes in residence time and recirculation structure govern the balance between NO_2 photolysis, O_3 production, and NO-driven titration processes within the canyon.

3.4. Convergence Analysis

In CFD simulations, achieving numerical convergence is a critical step to ensure that the solution is stable and reliable. To assess the convergence of the model, the residuals of various variables were tracked during the simulation iterations. Residuals represent the difference between successive iterations, and their reduction indicates that the solution is approaching a steady state. The lower the residual values, the closer the solution is to convergence, and thus the greater the accuracy of the simulation results [30, 48]. Figures 6 and 7 show the residuals for the model with and without obstacles, respectively.

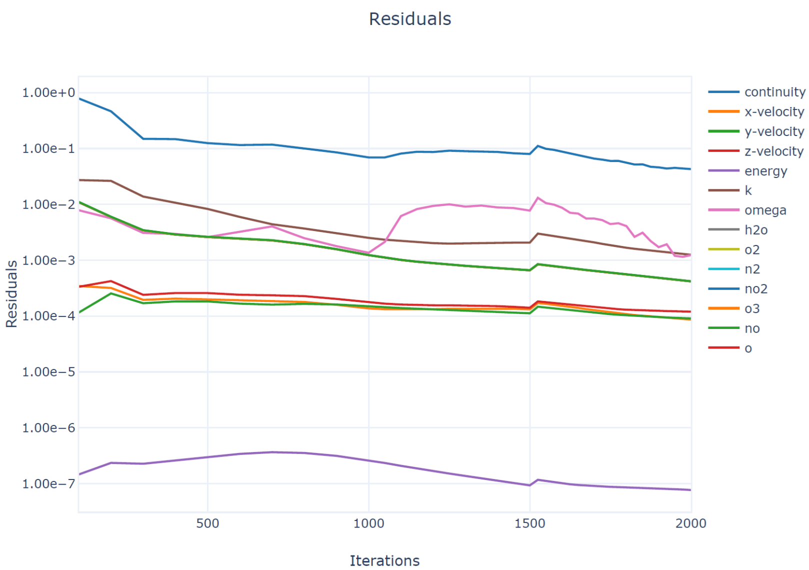

Figure 6. Residual histories of the k–ω SST model for the with-obstacle configuration, showing the convergence behavior of flow, turbulence, energy, and reactive species variables.

In both cases, residuals for key variables such as velocity components (x, y, z), energy, turbulence (k, ω), and reactive species (NO_2, O_3, etc.) decrease as the number of iterations increases. The continuity residual exhibits the highest value initially but decreases steadily to a level below 10^{-4}, indicating that mass conservation is effectively achieved in both configurations. The residuals for velocity components and energy also exhibit similar trends, reaching steady values indicating that the flow field and energy balance are well-converged.

In the with-obstacle scenario (Figures 6), the residuals of the reactive species like NO_2, O_3, and NO show a stable trend and decrease below 10^{-4} by around 1,500 iterations. This demonstrates that the model achieved

Figure 7. Residual histories of the k–ω SST model for the without-obstacle configuration, showing the convergence behavior of flow, turbulence, energy, and reactive species variables.

convergence in capturing the transport and chemical reactions of the pollutants in the street canyon with obstacles. In the without-obstacle case (Figure 7), the residuals for similar variables also converge at a similar rate, although the overall decay is slightly slower, indicating that the lack of obstacles leads to a less complex flow regime and possibly faster convergence of the simulation. Both models, with and without obstacles, show that the simulation reached numerical convergence after approximately 1,500 iterations, with residuals stabilized below 10^{-4} for all variables. This confirms the reliability of the results for both configurations.

In conclusion, the convergence analysis shows that the simulations for both configurations have reached a stable and accurate solution. The reduction in residuals indicates that the model was numerically convergent, allowing for reliable interpretation of airflow dynamics and pollutant distribution in the street canyon. These results validate the numerical approach used for this study and ensure that the subsequent analysis of pollutant transport is based on a stable and reliable solution.

3.5. Model validation

To assess the reliability of the CFD model, a limited field comparison was carried out using NO_2 and O_3 measurements collected along Jl. Dr. Ir. H. Soekarno, Surabaya, at three representative sampling points (Point 1–Point 3) during a three-day sampling campaign. These locations were selected to capture pollutant variability along the analyzed street-canyon segment. The sampling points were mapped onto the computational domain to enable comparison with the simulated results. However, because physical access to the actual upstream boundary of the CFD domain was limited during field sampling, Point 1 was not located exactly at the prescribed inlet plane. Instead, Point 1 was selected as the nearest accessible roadside location on the upstream side of the study segment and is therefore treated as a near-inlet roadside proxy rather than a direct representation of the CFD inlet boundary. Point 2 and Point 3 correspond to the internal canyon locations represented by Street 1 and Street 2, respectively. The observed concentrations were averaged over the measurement period to obtain representative values for comparison. Accordingly, the comparison presented in Table 7 should be interpreted as a limited field-based evaluation under practical sampling constraints rather than as a strict one-to-one validation of the prescribed boundary conditions.

Table 7. Comparison between observed and simulated pollutant concentrations under the obstacle configuration

Location	**Observed NO_2** (μg/m^3)	**Simulated NO_2** (μg/m^3)	**Observed O_3** (μg/m^3)	**Simulated O_3** (μg/m^3)
Point 1 (near-inlet proxy)	118.82	18.53	0.39	50.21
Point 2 (Street 1)	86.99	9.21	0.83	2.99
Point 3 (Street 2)	160.46	8.04	0.78	5.72

To quantitatively describe the discrepancy between measured and simulated concentrations, two statistical indicators were used: Mean Absolute Error (MAE) and Root Mean Square Error (RMSE). These metrics are reported here as error indicators for a limited set of spatially averaged observations. They are defined as follows:

$$\text{MAE} = \frac{1}{n}\sum_{i=1}^{n} |C_{\text{sim},i} - C_{\text{obs},i}| \tag{38}$$

$$\text{RMSE} = \sqrt{\frac{1}{n}\sum_{i=1}^{n} (C_{\text{sim},i} - C_{\text{obs},i})^2} \tag{39}$$

The comparison reveals substantial discrepancies between simulated and observed concentrations, as reflected by the high MAE and RMSE values for both NO_2 and O_3 [36, 44] (Table 8). In particular, the model systematically underestimates NO_2 concentrations by approximately 84–95% across all three sampling points, while overestimating O_3 concentrations at the near-inlet proxy location and within the canyon. These results indicate the presence of a strong systematic discrepancy between the simplified CFD representation and the field measurements.

The discrepancy at Point 1 is partly attributable to the difference between the prescribed CFD inlet boundary and the actual accessible roadside sampling position. In the CFD model, the inlet represents an idealized upstream background condition, whereas the field measurement at Point 1 was collected at a roadside location that remained influenced by local traffic emissions and near-road chemical processes, including rapid O_3 titration by freshly emitted NO. In particular, the observed O_3 at Point 1 was only 0.39 µg/m^3, which is consistent with strong near-source NO-titration suppressing ambient O_3 at a roadside location with heavy traffic. The CFD inlet, by contrast, imposes a background O_3 value of 50.21 µg/m^3 derived from the SUF 6 monitoring station located in Wonorejo, which is positioned away from immediate traffic influence. This representational mismatch between the inlet boundary condition and the near-road measurement environment is the primary source of the overestimation at Point 1 and is expected rather than indicative of a fundamental model deficiency.

Additional disagreement within the canyon can be attributed to several modeling limitations. First, the chemical mechanism employed in this study is simplified and includes only NO_x–O_3 interactions without accounting for volatile organic compounds (VOCs), which play a critical role in urban ozone formation. The omission of VOC chemistry limits the model's ability to capture NO_x–VOC–O_3 sensitivity and may place greater emphasis on ozone production through NO_2 photolysis. Second, the representation of roadside vegetation as simplified solid obstacles affects airflow patterns and pollutant dispersion but does not account for aerodynamic drag, permeability effects, and turbulence production associated with porous vegetation canopies [18, 39]. Third, uncertainties in emission rates, temporal variability of traffic conditions, and atmospheric boundary conditions may also contribute to the observed discrepancies.

Table 8. Statistical validation metrics for NO_2 and O_3 concentrations

Pollutant	**MAE (μg/m^3)**	**RMSE (μg/m^3)**
NO_2	110.16	114.55
O_3	18.97	28.90

Furthermore, the field measurements reflect transient atmospheric conditions over three sampling days, whereas the present simulation assumes steady-state flow, constant emission input, and prescribed reaction rates. This difference in temporal representation introduces additional uncertainty into the comparison. The steady-state assumption in particular implies that diurnal variations in wind speed, temperature, solar radiation, and traffic volume are not resolved, whereas the observed concentrations integrate all of these time-varying effects over the sampling period. Moreover, because the validation dataset consists of only three spatially averaged sampling locations, the reported statistical metrics should be interpreted with caution. Overall, the present comparison indicates that the model should be interpreted primarily as a simplified qualitative tool for analyzing how obstacle-induced flow modification affects reactive pollutant transport in a tropical street canyon, rather than as a predictive model for exact concentration levels at the site.

4. Conclusion

The simulations show that urban obstacles significantly modify the aerodynamic structure of the tropical street canyon. In the obstacle configuration, broader high-pressure zones developed on the windward facades and stronger low-pressure regions appeared on the leeward side, indicating enhanced flow separation and wake effects. The velocity field further shows that the simplified roadside obstacles redistribute airflow within the canyon, producing localized acceleration in confined passages while reducing the overall ventilation performance. These flow modifications increase pollutant residence time and contribute to higher NO_2 and O_3 concentrations within the canyon compared with the non-obstacle case.

Overall, the results demonstrate that obstacle-induced flow modification plays an important role in shaping reactive NO_2–O_3 transport in tropical street canyons. However, the roadside green strips were represented as simplified solid obstacles rather than porous vegetation canopies, and the chemical mechanism was limited to NO_x–O_3 interactions without VOC chemistry. Therefore, the results should be interpreted as a simplified representation of coupled flow–chemistry behavior under the present modeling assumptions. Future research should incorporate porous-medium vegetation models, more comprehensive chemical mechanisms, and additional urban configurations to improve the physical realism and applicability of the framework for urban air-quality assessment.

Acknowledgement

The authors are grateful to the Indonesian Education Scholarship (Beasiswa Pendidikan Indonesia, BPI), the Center for Higher Education Funding and Assessment (Pusat Pembiayaan dan Asesmen Pendidikan Tinggi, PPAPT), and the Indonesia Endowment Fund for Education (Lembaga Pengelola Dana Pendidikan, LPDP), for supporting this research.

REFERENCES

1. K. D. Kanniah, D. G. Kaskaoutis, H. San Lim, M. T. Latif, N. A. F. Kamarul Zaman, and J. Liew, *Overview of atmospheric aerosol studies in Malaysia: Known and unknown*, Atmospheric Research, vol. 182, pp. 302–318, 2016. Doi: 10.1016/j.atmosres.2016.08.002
2. M. de F. Andrade, P. Kumar, E. D. de Freitas, R. Y. Ynoue, J. Martins, L. D. Martins, T. Nogueira, P. Perez-Martinez, R. M. de Miranda, T. Albuquerque, F. L. T. Gonçalves, B. Oyama, and Y. Zhang, *Air quality in the megacity of São Paulo: Evolution over the last 30 years and future perspectives*, Atmospheric Environment, vol. 159, pp. 66–82, 2017. Doi: 10.1016/j.atmosenv.2017.03.051
3. C. Li, Z. Wang, B. Li, Z.-R. Peng, and Q. Fu, *Investigating the relationship between air pollution variation and urban form*, Building and Environment, vol. 147, pp. 559–568, 2019. Doi: 10.1016/j.buildenv.2018.06.038
4. R. Ed-Daoudi, S. E. Khamlichi, and B. Ettaki, *A hybrid Machine Learning approach for air quality prediction in Morocco: combining CatBoost with metaheuristic optimization algorithms*, Statistics, Optimization and Information Computing, vol. 14, no. 5, pp. 2445–2471, 2025. Doi: 10.19139/soic-2310-5070-2705
5. S.-J. Mei, Z. Luo, F.-Y. Zhao, and H.-Q. Wang, *Street canyon ventilation and airborne pollutant dispersion: 2-D versus 3-D CFD simulations*, Sustainable Cities and Society, vol. 50, p. 101700, 2019. Doi: 10.1016/j.scs.2019.101700
6. P. Ghobadi, and N. Nasrollahi, *Assessment of pollutant dispersion in deep street canyons under different source positions: Numerical simulation*, Urban Climate, vol. 40, p. 101027, 2021. Doi: 10.1016/j.uclim.2021.101027

7. C. H. Sin, Y. Luo, K. S. Jon, P.-Y. Cui, and Y. Huang, *Effects of void deck on the airflow and pollutant dispersion in 3D street canyons*, Environmental Science and Pollution Research, vol. 29, no. 59, pp. 89358–89386, 2022. Doi: 10.1007/s11356-022-21827-1
8. A. Heidari, Y. Peyvastehgar, H. Eskandari, and E. Mansourian, *The effect of balcony configurations on ACH and pollutant concentration in symmetrical and asymmetrical street canyons*, Scientific Reports, vol. 15, no. 1, p. 8894, 2025. Doi: 10.1038/s41598-025-93736-5
9. X. Li, S. A. Hussain, S. Sobri, and M. S. M. Said, *Overviewing the air quality models on air pollution in Sichuan Basin, China*, Chemosphere, vol. 271, p. 129502, 2021. Doi: 10.1016/j.chemosphere.2020.129502
10. A. Badia, V. Vidal, S. Ventura, R. Curcoll, R. Segura, and G. Villalba, *Modelling the impacts of emission changes on O_3 sensitivity, atmospheric oxidation capacity, and pollution transport over the Catalonia region*, Atmospheric Chemistry and Physics, vol. 23, no. 18, pp. 10751–10774, 2023. Doi: 10.5194/acp-23-10751-2023
11. G. Wang, S. Bai, and J. M. Ogden, *Identifying contributions of on-road motor vehicles to urban air pollution using travel demand model data*, Transportation Research Part D: Transport and Environment, vol. 14, no. 3, pp. 168–179, 2009. Doi: 10.1016/j.trd.2008.11.011
12. A. F. Assomadi, J. Hermana, and B. Widodo, *Pendekatan baru model distribusi pencemar di atmosfer perkotaan*, Dissertation, Institut Teknologi Sepuluh Nopember (ITS), Surabaya, Indonesia, 2016.
13. S. Vranckx, P. Vos, B. Maiheu, and S. Janssen, *Impact of trees on pollutant dispersion in street canyons: A numerical study of the annual average effects in Antwerp, Belgium*, Science of The Total Environment, vol. 532, pp. 474–483, 2015. Doi: 10.1016/j.scitotenv.2015.06.032
14. F. Hsu and A. Bennett, *The effects of roadside buildings roof shapes and tree plantings on the vehicle exhaust gas pollution dispersion in the urban street*, Journal of Physics: Conference Series, vol. 2441, no. 1, p. 012010, 2023. Doi: 10.1088/1742-6596/2441/1/012010
15. C. Girotti, P. S. A. Matos, A. R. Prata Shimomura, F. A. Kurokawa, E. Correia, and A. Lopes, *Microclimate simulation and lichen-based validation analyzing street trees' impact on atmospheric pollutant dispersion at the urban canyon scale*, Urban Climate, vol. 62, p. 102549, 2025. Doi: 10.1016/j.uclim.2025.102549
16. S.-J. Park, J.-J. Kim, M. J. Kim, R. J. Park, and H.-B. Cheong, *Characteristics of flow and reactive pollutant dispersion in urban street canyons*, Atmospheric Environment, vol. 108, pp. 20–31, 2015. Doi: 10.1016/j.atmosenv.2015.02.065
17. Z. T. Ai and C. M. Mak, *CFD simulation of flow in a long street canyon under a perpendicular wind direction: Evaluation of three computational settings*, Building and Environment, vol. 114, pp. 293–306, 2017. Doi: 10.1016/j.buildenv.2016.12.032
18. C. Gromke, B. Blocken, W. Janssen, B. Merema, T. van Hooff, and H. Timmermans, *CFD analysis of transpirational cooling by vegetation: Case study for specific meteorological conditions during a heat wave in Arnhem, Netherlands*, Building and Environment, vol. 83, pp. 11–26, 2015. Doi: 10.1016/j.buildenv.2014.04.022
19. Z. Tong, R. W. Baldauf, V. Isakov, P. Deshmukh, and K. Max Zhang, *Roadside vegetation barrier designs to mitigate near-road air pollution impacts*, Science of The Total Environment, vol. 541, pp. 920–927, 2016. Doi: 10.1016/j.scitotenv.2015.09.067
20. Z. Eslamidoost, M. R. Samaei, H. Hashemi, M. A. Baghapour, M. Arabzadeh, S. Dehghani, and S. Rajabi, *Assessment of air quality using AERMOD modeling: a case study in the Middle East*, Environmental Monitoring and Assessment, vol. 195, no. 11, p. 1272, 2023. Doi: 10.1007/s10661-023-11879-2
21. D. Yang, M. Li, and H. Liu, *A Parallel Computing Algorithm for the Emergency-Oriented Atmospheric Dispersion Model CALPUFF*, Atmosphere, vol. 13, no. 12, p. 2129, 2022. Doi: 10.3390/atmos13122129
22. J. I. Huertas and D. F. Prato, *CFD modeling of near-roadway air pollution*, Environmental Modeling & Assessment, vol. 25, no. 1, pp. 129–145, 2020. Doi: 10.1007/s10666-019-09666-w
23. J. Zhong, X.-M. Cai, and W. J. Bloss, *Modelling photochemical pollutants in a deep urban street canyon: Application of a coupled two-box model approximation*, Atmospheric Environment, vol. 143, pp. 86–107, 2016. Doi: 10.1016/j.atmosenv.2016.08.027
24. N. Ridzuan, U. Ujang, S. Azri, and T. L. Choon, *Visualising urban air quality using aermod, calpuff and cfd models: A critical review*, The International Archives of the Photogrammetry, Remote Sensing and Spatial Information Sciences, vol. XLIV-4-W3-2020, pp. 355–363, 2020. Doi: 10.5194/isprs-archives-XLIV-4-W3-2020-355-2020
25. T. Lauriks, R. Longo, D. Baetens, M. Derudi, A. Parente, A. Bellemans, J. van Beeck, and S. Denys, *Application of improved CFD modeling for prediction and mitigation of traffic-related air pollution hotspots in a realistic urban street*, Atmospheric Environment, vol. 246, p. 118127, 2021. Doi: 10.1016/j.atmosenv.2020.118127
26. J. Franke, A. Hellsten, H. Schlünzen, and B. Carissimo, *Best practice guideline for the CFD simulation of flows in the urban environment*, COST European Cooperation in Science and Technology, Hamburg, 2007. Available: https://hal.science/hal-04181390v1
27. F. R. Menter, *Two-equation eddy-viscosity turbulence models for engineering applications*, AIAA Journal, vol. 32, no. 8, pp. 1598–1605, 1994. Doi: 10.2514/3.12149
28. B. Blocken, *Computational Fluid Dynamics for urban physics: Importance, scales, possibilities, limitations and ten tips and tricks towards accurate and reliable simulations*, Building and Environment, vol. 91, pp. 219–245, 2015. Doi: 10.1016/j.buildenv.2015.02.015
29. J.-J. Baik, Y.-S. Kang, and J.-J. Kim, *Modeling reactive pollutant dispersion in an urban street canyon*, Atmospheric Environment, vol. 41, no. 5, pp. 934–949, 2007. Doi: 10.1016/j.atmosenv.2006.09.018
30. H. K. Versteeg and W. Malalasekera, *An introduction to computational fluid dynamics: The finite volume method*, Pearson Education Limited, England, 2007.
31. W. B. DeMore, S. P. Sander, D. M. Golden, R. F. Hampson, M. J. Kurylo, C. J. Howard, A. R. Ravishankara, C. E. Kolb, and M. J. Molina, *Chemical kinetics and photochemical data for use in stratospheric modeling*, Jet Propulsion Laboratory, NASA, California, JPL Publication 97-4, 1997.
32. W. H. Swartz, *Photolysis rate coefficient calculations in support of SOLVE II*, Final Report: Summary of Research for NASA Grant NNG04GH56G, The Johns Hopkins University Applied Physics Laboratory, 2005. Available: https://ntrs.nasa.gov/citations/20050167079
33. R. R. Dickerson, D. H. Stedman, and A. C. Delany, *Direct measurements of ozone and nitrogen dioxide photolysis rates in the troposphere*, Journal of Geophysical Research: Oceans, vol. 87, no. C7, pp. 4933–4946, 1982. Doi: 10.1029/JC087iC07p04933

34. J. Guan, S. Solomon, S. Madronich, and D. Kinnison, *Inferring the photolysis rate of NO_2 in the stratosphere based on satellite observations*, Atmospheric Chemistry and Physics, vol. 23, no. 18, pp. 10413–10422, 2023. Doi: 10.5194/acp-23-10413-2023
35. K. J. Laidler, *A glossary of terms used in chemical kinetics, including reaction dynamics (IUPAC Recommendations 1996)*, Pure and Applied Chemistry, vol. 68, no. 1, pp. 149–192, 1996. Doi: 10.1351/pac199668010149
36. A. Baklanov, L. T. Molina, and M. Gauss, *Megacities, air quality and climate*, Atmospheric Environment, vol. 126, pp. 235–249, 2016. Doi: 10.1016/j.atmosenv.2015.11.059
37. Y. Tominaga and T. Stathopoulos, *CFD modeling of pollution dispersion in building array: Evaluation of turbulent scalar flux modeling in RANS model using LES results*, Journal of Wind Engineering and Industrial Aerodynamics, vol. 104–106, pp. 484–491, 2012. Doi: 10.1016/j.jweia.2012.02.004
38. A. P. R. Jeanjean, P. S. Monks, and R. J. Leigh, *Modelling the effectiveness of urban trees and grass on $PM_{2.5}$ reduction via dispersion and deposition at a city scale*, Atmospheric Environment, vol. 147, pp. 1–10, 2016. Doi: 10.1016/j.atmosenv.2016.09.033
39. R. Buccolieri, C. Gromke, S. Di Sabatino, and B. Ruck, *Aerodynamic effects of trees on pollutant concentration in street canyons*, Science of The Total Environment, vol. 407, no. 19, pp. 5247–5256, 2009. Doi: 10.1016/j.scitotenv.2009.06.016
40. J. Hang, Y. Li, M. Sandberg, R. Buccolieri, and S. Di Sabatino, *The influence of building height variability on pollutant dispersion and pedestrian ventilation in idealized high-rise urban areas*, Building and Environment, vol. 56, pp. 346–360, 2012. Doi: 10.1016/j.buildenv.2012.03.023
41. F. R. Sarria, Mc. G. Delgado, R. M. Palma, T. P. Amores, J. S. Ramos, and S. Á. Domínguez, *Modelling pollutant dispersion in urban canyons to enhance air quality and urban planning*, Applied Sciences, vol. 15, no. 4, p. 1752, 2025. Doi: 10.3390/app15041752
42. T. R. Oke, *Street design and urban canopy layer climate*, Energy and Buildings, vol. 11, no. 1, pp. 103–113, 1988. Doi: 10.1016/0378-7788(88)90026-6
43. K.-H. Kwak, and J.-J. Baik, *A CFD modeling study of the impacts of NO_x and VOC emissions on reactive pollutant dispersion in and above a street canyon*, Atmospheric Environment, vol. 46, pp. 71–80, 2012. Doi: 10.1016/j.atmosenv.2011.10.024
44. S. Vardoulakis, B. E. A. Fisher, K. Pericleous, and N. Gonzalez-Flesca, *Modelling air quality in street canyons: A review*, Atmospheric Environment, vol. 37, no. 2, pp. 155–182, 2003. Doi: 10.1016/S1352-2310(02)00857-9
45. D. J. Nowak, S. Hirabayashi, A. Bodine, and E. Greenfield, *Tree and forest effects on air quality and human health in the United States*, Environmental Pollution, vol. 193, pp. 119–129, 2014. Doi: 10.1016/j.envpol.2014.05.028
46. P. S. Monks, A. T. Archibald, A. Colette, O. Cooper, M. Coyle, R. Derwent, D. Fowler, C. Granier, K. S. Law, G. E. Mills, D. S. Stevenson, O. Tarasova, V. Thouret, E. von Schneidemesser, R. Sommariva, O. Wild, and M. L. Williams, *Tropospheric ozone and its precursors from the urban to the global scale from air quality to short-lived climate forcer*, Atmospheric Chemistry and Physics, vol. 15, no. 15, pp. 8889–8973, 2015.
47. J. H. Seinfeld, and S. N. Pandis, *Atmospheric chemistry and physics: From air pollution to climate change, 3rd ed*, John Wiley & Sons, Inc, USA, 2016.
48. D. C. Wilcox, *Turbulence modeling for CFD*, DCW Industries, California, 2006.